Melt Pool characteristics on surface roughness and printability of 316L stainless steel in laser powder bed fusion

Tianyu Zhang and Lang Yuan
Department of Mechanical Engineering, University of South Carolina, Columbia, South Carolina, USA

Abstract

Purpose – Surface quality and porosity significantly influence the structural and functional properties of the final product. This study aims to establish and explain the underlying relationships among processing parameters, top surface roughness and porosity level in additively manufactured 316L stainless steel.

Design/methodology/approach – A systematic variation of printing process parameters was conducted to print cubic samples based on laser power, speed and their combinations of energy density. Melt pool morphologies and dimensions, surface roughness quantified by arithmetic mean height (Sa) and porosity levels were characterized via optical confocal microscopy.

Findings – The study reveals that the laser power required to achieve optimal top surface quality increases with the volumetric energy density (VED) levels. A smooth top surface (Sa $< 15\ \mu$m) or a rough surface with humps at high VEDs (VED $>$ 133.3 J/mm^3) can serve as indicators for fully dense bulk samples, while rough top surfaces resulting from melt pool discontinuity correlate with high porosity levels. Under insufficient VED, melt pool discontinuity dominates the top surface. At high VEDs, surface quality improves with increased power as mitigation of melt pool discontinuity, followed by the deterioration with hump formation.

Originality/value – This study reveals and summarizes the formation mechanism of dominant features on top surface features and offers a potential method to predict the porosity by observing the top surface features with consideration of processing conditions.

Keywords Additive manufacturing, Porosity, Surface roughness, Hump, Melt pool discontinuity

Paper type Research paper

1. Introduction

The laser powder bed fusion (L-PBF) process, as a prominent metal-based additive manufacturing (AM) technology, affords a high degree of freedom in realizing intricate geometrical designs and fostering location-specific microstructures. Its applications span diverse industries, including aerospace, automotive and medical equipment manufacturing (Fu *et al.*, 2022; Wang *et al.*, 2011). A comprehensive understanding of melt pool characteristics at different processing parameters and their impacts on product quality builds the foundation to achieve customized functional and structural properties (Cook and Murphy, 2020; Ghosh *et al.*, 2018; Liu and Du Pont, 2004; Teng *et al.*, 2017). Specifically, the surface roughness, which is highly impacted by the melt pool morphology (Cabanettes *et al.*, 2018; Mumtaz and Hopkinson, 2009; Triantaphyllou *et al.*, 2015), not only influences the geometrical tolerances of the product but also determines the mechanical properties such as fatigue life (Hu *et al.*, 2024; Liao *et al.*, 2020; Maleki *et al.*, 2023) and functional behaviors such as heat transfer efficiency (Rastan *et al.*, 2020; Thompson *et al.*, 2015; Zhu *et al.*, 2020) of the products. Additionally, the morphology of the melt pool plays a pivotal role in shaping defects during the printing process, thereby influencing the overall quality of the product (Bauereiß *et al.*, 2014; Leung *et al.*, 2018; Tang *et al.*, 2018).

Previous research has established a robust correlation between melt pool dimensions and morphologies with processing parameters. Yang *et al.* (2016) explored the impact of scanning speed, laser power and layer thickness on melt pool mode and morphology of Ti-6Al-4V in L-PBF. The results revealed that scanning speed exerted the most significant

The current issue and full text archive of this journal is available on Emerald Insight at: **https://www.emerald.com/insight/1355-2546.htm**

Rapid Prototyping Journal
© Emerald Publishing Limited [ISSN 1355-2546]
[DOI 10.1108/RPJ-02-2024-0078]

The authors would like to acknowledge the support from the National Science Foundation under grant number 2029425, and Savannah River National Laboratory under Contract No. 89303321CEM000080 for the U.S. Department of Energy.

Declaration of interests: The authors declare that they have no known competing financial interests or personal relationships that could have appeared to influence the work reported in this paper.

The authors declare the following financial interests/personal relationships which may be considered as potential competing interests.

Lang Yuan reports financial support provided by National Science Foundation. Lang Yuan reports financial support was provided by Savannah River National Laboratory. If there are other authors, they declare that they have no known competing financial interests or personal relationships that could have appeared to influence the work reported in this paper.

Received 14 February 2024
Revised 16 May 2024
Accepted 27 June 2024

impact on melt pool morphology. As scanning speed increased, melt pool width, depth and depth-to-width ratio decreased. Yadroitsev *et al.* (2007) examined the effect of the power/speed ratio on melt pool behavior in stainless steel 904L using L-PBF. Their study found that the melt track width increased with higher power and decreased with increased scanning speed. Jing and Wang (2021) investigated the influence of varying laser power, hatch spacing and layer thickness on 300M steel through L-PBF. The study concluded that increased scanning speed and layer thickness resulted in a reduction in melt pool width. However, the melt pool depth exhibited no significant correlation with the changes in layer thickness.

Driven by the inherent physical phenomena occurring within the melt pool, such as recoil pressure, vaporization and the Marangoni effect (Dai and Gu, 2015a; Le and Lo, 2019; Semak and Matsunawa, 1997), the top surface topography of the melt pool exhibits distinctive features such as balling, humps and pores, thereby influencing the top surface roughness (Khairallah *et al.*, 2016; Matthews *et al.*, 2016; Soderstrom and Mendez, 2006; Tang *et al.*, 2020). Dai and Gu (2015b) found that molten material tended to move backward, accumulating at the rear of the melt pool, thereby increasing top surface roughness. Moreover, vaporization and spattering resulted in liquid loss during the melting process, while the shrinkage phenomenon during solidification contributed to pore formation on the top surface. Yadroitsev *et al.* (2010, 2013) observed the Plateau–Rayleigh instability of the melt pool under high-speed conditions. This capillary instability minimizes surface energy, resulting in an uneven surface. The observation aligns with the findings reported by Tian *et al.* (2017). Gu *et al.* (Gu and Shen, 2009) demonstrated two types of balling effects under different energy input conditions: one is limited liquid volume in low energy density conditions and another is melt spatters. Calignano *et al.* (2013) reported that scanning speed has the most significant impact on top surface roughness, followed by hatching distance and laser power. Yakout *et al.* (2017) concluded that increasing input energy density led to a better surface finish by eliminating the lack of fusion voids on the top surface. Shi *et al.* (2020) analyzed the impact of layer thickness on surface quality, density and tensile properties of Ti-6Al-4V. The results indicated that high layer thickness significantly deteriorated top surface roughness without substantially impacting density and tensile properties.

Despite extensive studies on top surface features and melt pool morphology, a comprehensive investigation covering a broad spectrum of laser power and scanning speed settings is notably absent, hindering a holistic understanding of melt pool behavior. Moreover, the specific features that govern top surface roughness under varying energy density conditions remain inadequately understood. This study aims to bridge these gaps by exploring the relationship between processing parameters and melt pool characteristics across a wide range of laser power (80 W to 800 W) and scanning speed (160 mm/s to 4,000 mm/s). Concurrently, the study explores the interconnections among melt pool morphology, top surface roughness and bulk porosity. As a result, the relationship between top surface roughness features and printability is discussed. This study not only contributes to a systematic understanding of melt pool behaviors but also establishes a guideline for selecting processing parameters in printing 316L stainless steel with L-PBF. Furthermore, a promising avenue for assessing porosity levels during printing by analyzing surface topography is proposed based on this experiment result.

2. Experimental methodology

Cubic samples with the size of 10 mm × 10 mm × 10 mm were fabricated using stainless steel 316L powder by the AconityMIDI L-PBF printer. The powder, with a particle size distribution ranging from 15 μm to 45 μm and a mean value of 30 μm, was supplied by Carpenter Technology Corporation. The study comprised six sample groups, denoted as Groups 1–6. Groups 1–4 were structured based on a constant volumetric energy density (VED), defined as:

$$VED = \frac{P}{Th \times S \times H} \tag{1}$$

where P is laser power, Th is layer thickness, S is laser scanning speed and H is hatch spacing. The specific VED values chosen for these groups were 66.7 J/mm^3, 100 J/mm^3, 133.3 J/mm^3, 166.7 J/mm^3. Five levels of laser powers (80 W, 260 W, 440 W, 620 W and 800 W) were utilized within each group, covering the machine's broadest power range. Scanning speeds were then calculated by equation (1) to maintain a constant VED, spanning an extensive range from 160 mm/s to 4,000 mm/s. To further explore the influence of laser speed, two additional groups, Groups 5 and 6, were introduced by adding two points each at the power of 260 W and 620 W, respectively. Scanning speeds for Groups 5 and 6 were fixed at 1,100 mm/s and 1,466.6 mm/s, respectively. This experimental design allowed comparative analysis, emphasizing the impact of energy density, laser scanning speed and laser power on the fabricated samples. Figure 1 illustrates all the conditions. A naming convention based on power and speed is used in this study to better refer to the process conditions. For example, a sample labeled P260_S1300 corresponds to a configuration with a laser power of 260 W and a scanning speed of 1,300 mm/s.

The selection of laser power and scanning speed covers the practical parametric space in production (Cook and Ritchie, 2023) and delves into the relatively less-explored realm of high laser power region, specifically beyond 400 W for 316L stainless steel in L-PBF. Throughout the printing process, the layer thickness, laser spot size and hatch spacing were maintained at constants of 30 μm, 100 μm, and 100 μm, respectively. A simple hatching strategy, where the laser scans back and forth across the entire sample, is applied with a 90° rotation angle between the consecutive layers. Subsequent to the hatch scans, a single contour scan, preserving the same parameters as the hatch scans, was executed on each layer with a 50 μm offset distance. All samples were printed under an argon gas environment with an oxygen level below 100 ppm to minimize oxidation. Each sample was printed twice to ensure the repeatability of the data. If a considerable variation is notable under the same process condition, a third sample was printed to double confirm the result. The printed samples on the build plate are shown in Figure 2(a).

The top surface topography was assessed using the Keyence VHX-5000 digital optical microscope. The height data, $Z(x, y)$, was acquired to quantify the surface roughness, presented by

Figure 1 Process conditions

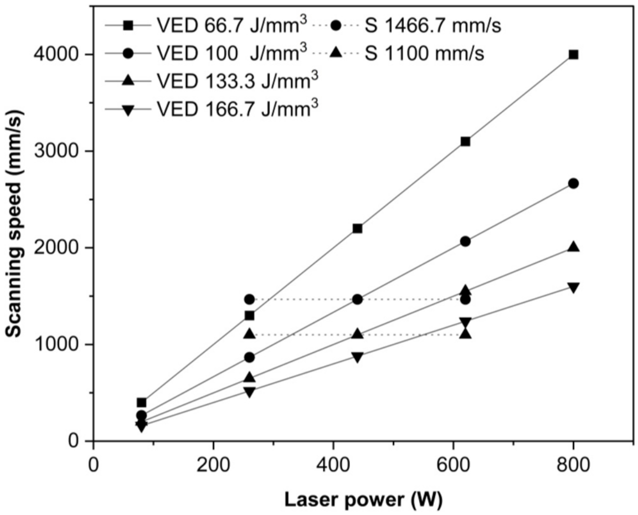

Notes: VED: volumetric energy density; S: laser scanning speed
Source: Authors' own work

the arithmetical mean height of the surface, Sa. It is calculated by:

$$Sa = \frac{1}{A}\iint_{A} |Z(x,y)|dxdy \qquad (2)$$

To visualize the melt pool morphology in cross-sections, samples underwent procedures of cutting, grinding, polishing and etching. The cutting plane was aligned perpendicular to the laser scanning direction on the top surface. The images for cubic samples after cutting and mounting are shown in Figure 2(b) and (c), respectively. For etching, a mixture of 75 vol% HCl and 25 vol% HNO_3 was used, with an etch time of 15 s. Melt pool width and depth were measured at least five times from the section view, and an average value was then computed, as illustrated in Figure 3. The build direction (BD) is indicated by the arrow in Figure 3. The porosity was quantified three times through different cross-sectional images from the same sample using the open-source tool ImageJ (Al Aridi *et al.*, 2024), further verified through the Archimedes method.

3. Results and discussion

3.1 Laser power on melt pool morphology

Figure 4 shows the melt pool morphology under various laser power conditions while maintaining the fixed scanning speeds of 1,466.6 mm/s and 1,100 mm/s for each column, respectively. Under the P260_S1466.6 [Figure 4(a)] condition, the melt pool width is comparable to or smaller than the hatching distance of 100 μm. The constrained width hinders effective connection with prior melt tracks, leading to poor wetting conditions. In addition, the relatively low energy input results in diminished melt pool temperature, causing elevated surface tension in 316L stainless steel (Leung *et al.*, 2019; Mills and Keene, 1990; Zhang and Yuan, 2022). Consequently, the combination of increased surface tension and poor wetting conditions facilitates the consolidation of the melt pool into a cross-sectional ellipse shape. With increased laser power to 440 and 620 W conditions, a larger volume of molten liquid can be generated at the consistent scanning speed of 1,466.6 mm/s, as shown in Figure 4(b) and (c). The augmented liquid volume improves wetting between the melt pool and previously solidified melt tracks, transforming the cross-sectional melt pool shape from an ellipse to a half-ellipse. A similar observation of the transformation can be noticed when the laser scanning speed is 1,100 mm/s, as illustrated in Figure 4(d–f).

Figure 2 Printed samples

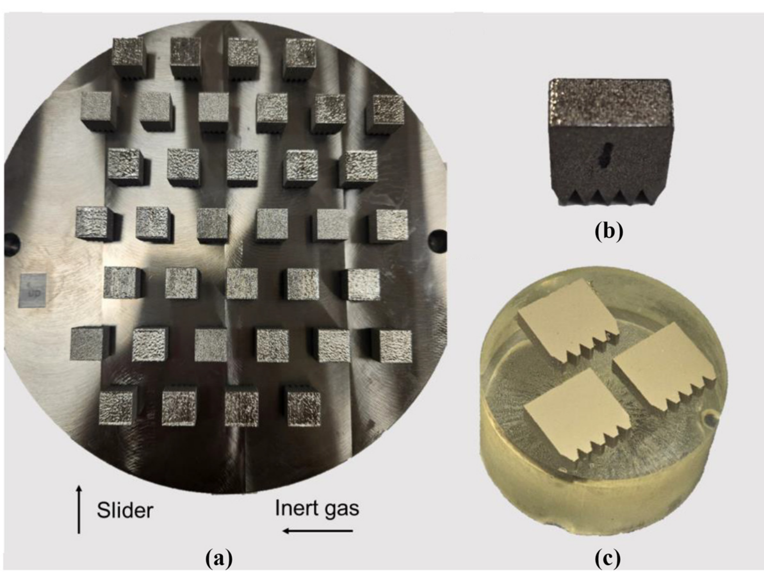

Notes: (a) Samples on the build plate; (b) a sample after cutting; (c) samples after mounting
Source: Authors' own work

Figure 3 Cross-sectional view of melt pools and their width and depth measurements

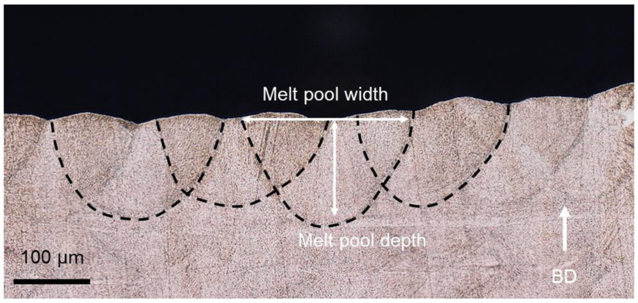

Source: Authors' own work

The quantified melt pool width and depth extracted from Figure 4 are presented in Figure 5. In each group, the increase in laser power causes increased melt pool width and depth, aligning with observations documented in the literature (Cook and Ritchie, 2023; Tangestani *et al.*, 2021). Notably, the melt pool depth exhibits a similar value between the 1,466.6 mm/s group and the 1,100 mm/s group under identical laser power conditions. Conversely, the melt pool width in the 1,100 mm/s group is significantly larger than that in the 1,466.6 mm/s group with the same laser power. The measurements indicate that reducing the scanning speed, thereby increasing VED, tends to widen the melt pool more than deepening it (also observed in Figure 4). This behavior can be elucidated by considering the Marangoni flow and denudation effect, which intricately govern the melt pool dynamics, as discussed in detail below.

The Marangoni effect significantly influences the shape of the melt pool by amplifying the liquid flow within it. As illustrated in Figure 6, the Marangoni flow arises due to differences in surface tension (σ) as a consequence of temperature variations. Liquid migrates from low to high surface tension regions (Le and Lo, 2019; Yin and Emi, 2003). In 316L stainless steel, the temperature coefficient is negative when the sulfur level is lower than 75 ppm, and the oxygen level is lower than 570 ppm (Leung *et al.*, 2019; Mills and Keene, 1990; Zhang and Yuan, 2022). The resulting Marangoni flow, therefore, is in the centrifugal direction, widening the melt pool through outward flow movement. At slower scanning speeds, a higher temperature is attained at the laser irradiation area. The increased thermal gradient between the melt pool center and boundary amplifies the Marangoni flow's strength. Moreover, the liquid viscosity decreases with higher temperatures, accelerating the Marangoni flow and culminating in a melt pool characterized by a broader but shallower shape.

In addition to the Marangoni flow, the denudation effect can also play a crucial role in reducing the dimensions of the melt pool

Figure 4 Melt pool morphology under fixed scanning speeds

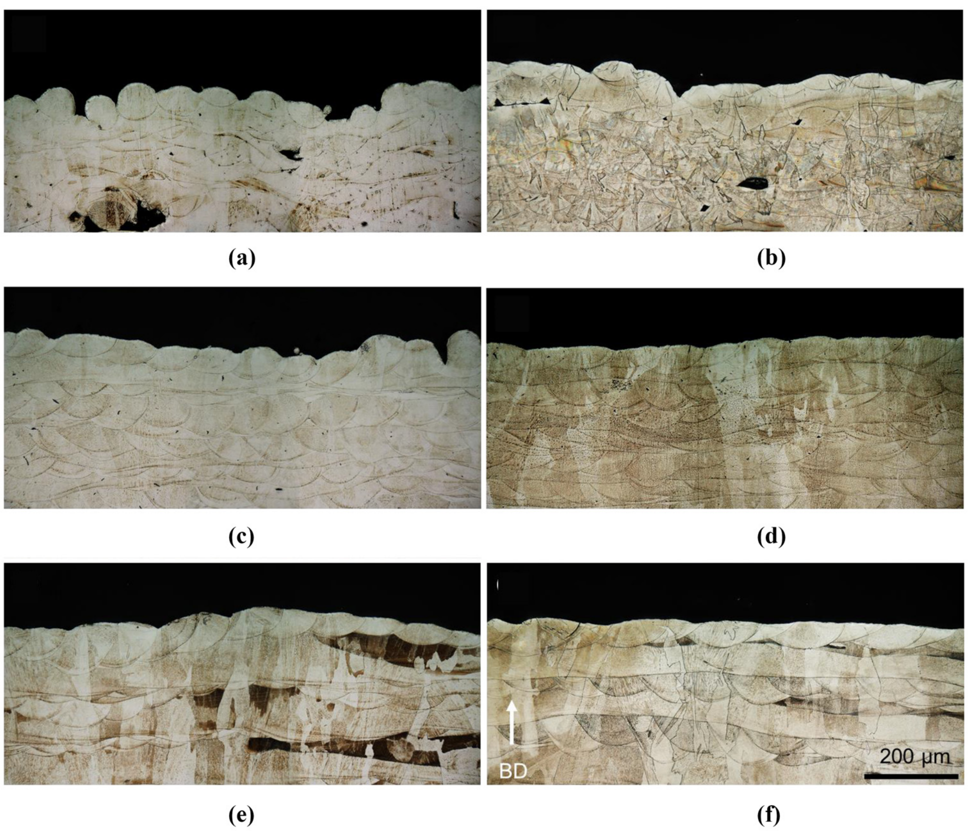

Notes: (a) P260_S1466.6; (b) P440_S1466.6; (c) P620_S1466.6; (d) P260_S1100; (e) P440_S1100; (f) P620_S1100.
Source: Authors' own work

Figure 5 Melt pool width and depth for fixed scanning speeds at 1,100 mm/s and 1,466.6 mm/s

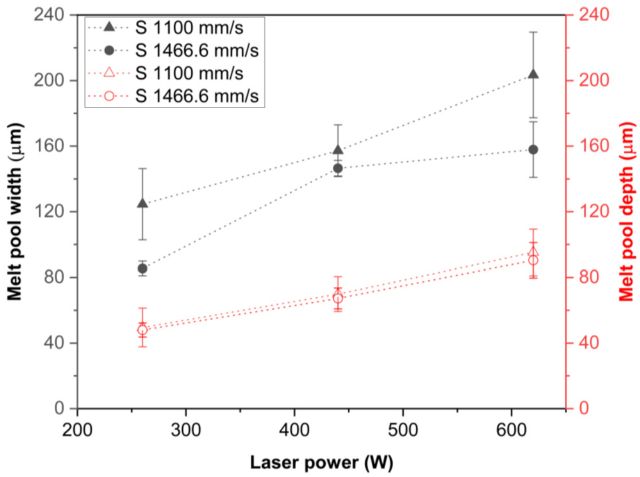

Source: Authors' own work

during the printing process. The denudation zone primarily originates from two mechanisms (Chen and Yan, 2020): powder ejection and melt pool oscillation. Both phenomena are associated with the recoil pressure during printing. Under the high-energy laser, a substantial amount of metal vapor expands, creating pressure on the free surface. The recoil pressure can be described using a simple model expressed as (Semak and Matsunawa, 1997):

$$P_r = A\ B_0 T_{surf}^{-1/2} \exp\left(-\frac{U}{kT_{surf}}\right) \tag{3}$$

where A is a coefficient dependent on ambient pressure and B_0 is an empirical constant. T_{surf} is the temperature of the local surface and U is the energy of evaporation of a single atom, which can be calculated by (Semak and Matsunawa, 1997):

$$U = M_a L_v / N_a k_b \tag{4}$$

where M_a is the atomic mass, L_v is the latent heat of evaporation, N_a is Avogadro's number and k_b is Boltzmann's constant. A higher VED input (corresponding to a higher laser power or lower scanning speed) leads to an elevated melt pool temperature and increased recoil pressure, as indicated by equation (4). The high-pressure metal vapor can displace the powder around the melt track, creating the denudation zone (Leung *et al.*, 2018; Wang *et al.*, 2017; Young *et al.*, 2020), as illustrated in Figure 6. Throughout the evaporation process, the recoil force undergoes fluctuations due to variations in the energy balance, which induces the melt pool oscillation and absorbs the nearby powder into the melt pool (Lei *et al.*, 2018). Subsequently, solidification shrinkage maintains the powder-free zone, resulting in an oscillation-induced denudation zone, as illustrated in Figure 6(b). The denudation effect displaces powder from the powder base, reducing the volume of melt liquid available for the next track. It also reduces the number of powder particles irradiated by the laser, resulting in lower laser absorption for the subsequent melt track (Fischer *et al.*, 2003). The combination of a reduced quantity of molten liquid and low laser absorption counteracts the increasing VED, impeding the expansion of the melt pool. Simultaneously, a reinforced Marangoni flow widens the melt pool, ultimately leading to a similar depth under elevated VED conditions.

3.2 Laser power on top surface roughness

Figure 7 illustrates the surface topography of different laser power levels at fixed scanning speeds of 1,100 mm/s and 1,466.6 mm/s, corresponding to Figure 4. Figure 7 quantifies the top surface roughness Sa. In general, the Sa decreases with increased laser power at identical laser scanning speed conditions. Under the 260 W conditions, insufficient laser power input leads to discontinuous (along laser scanning direction) and unconnected (between neighbor melt tracks) melt tracks on the top surface, as shown in Figure 7(a) and (d). In addition, partially melted powder particles are evident on the surface [seen in Figure 7(a) and (b)], contributing to the high Sa (20.66 μm for P260_S1466.6 and

Figure 6 The illustration of melt pool dynamics in melt pool formation

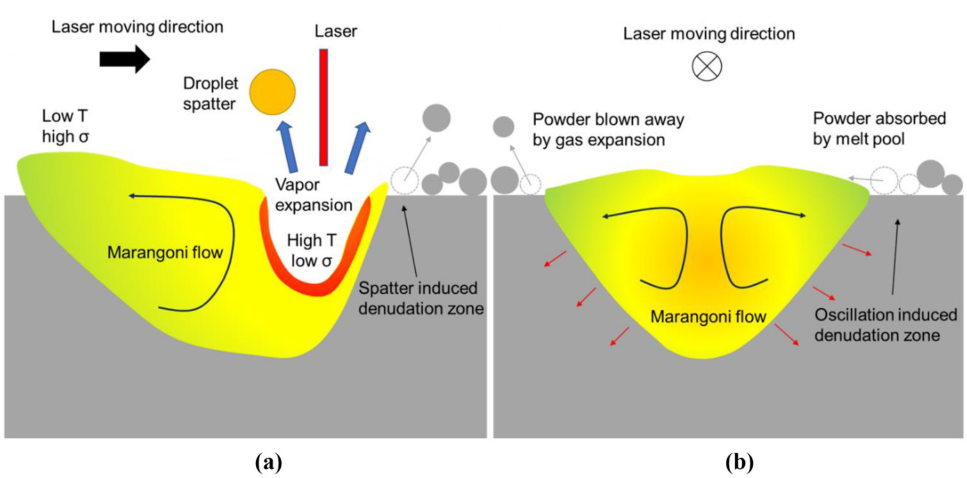

Source: Authors' own work

Figure 7 Top surface topography with fixed scanning speeds

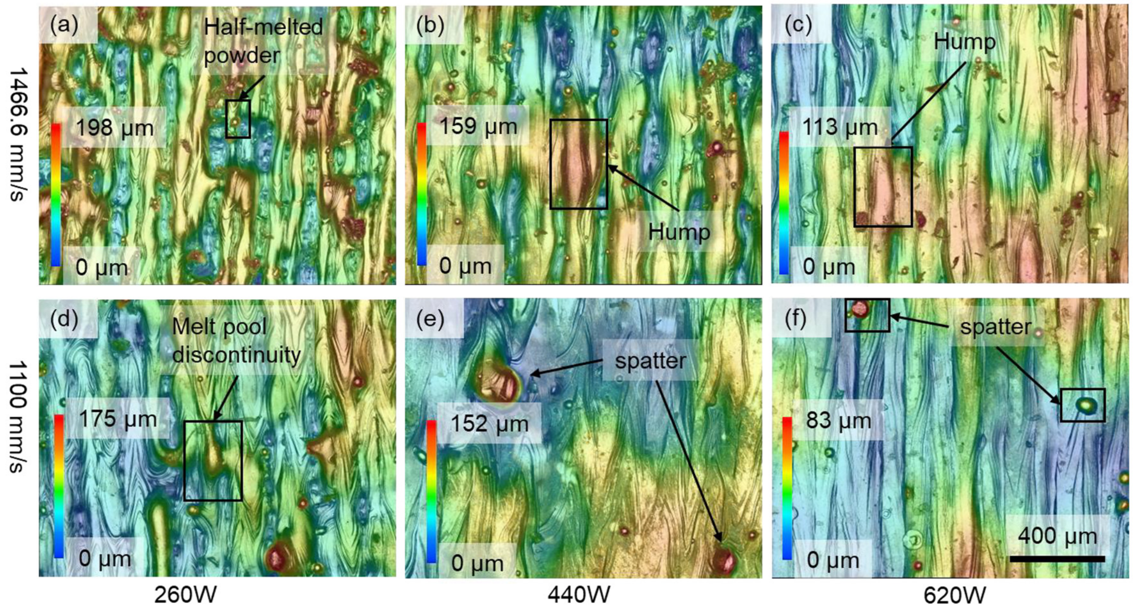

Notes: (a) P260_S1466.6; (b) P440_S1466.6; (c) P620_S1466.6; (d) P260_S1100; (e) P440_S1100; (f) P620_S1100.
Source: Authors' own work

18.45 μm for P260_S1100). In contrast, at the 620 W condition, a larger melt pool, caused by the increased energy density and intensified Marangoni flow, fosters overlaps among melt tracks and the previous layers, as shown in Figure 4(c) and (f). Such behavior reduces the contact angle and enhances wetting, yielding a flatter top surface. Furthermore, the lower surface tension and viscosity of the liquid at higher temperatures, coupled with a large melt volume, afford an extended solidification time and, in turn, facilitate gravity and centrifugal Marangoni flow, contributing to a reduction of protrusion height and a smoother top surface (Leung *et al.*, 2022). Consequently, at the same scanning speed, the Sa value reduces from 20.66 μm and 18.55 μm at 260 W conditions to 18.45 μm and 10.32 μm at 620 W conditions, respectively, as shown in Figure 7(a), (c–d) and (f).

Despite the overall improvement in top surface roughness, higher laser power levels tend to induce spatter formation under relatively high VED conditions. The increased laser power enhances fluid circulation velocity within the melt pool due to higher recoil pressure and a more pronounced Marangoni flow. When the recoil pressure surpasses the surface tension of the molten liquid, droplet spatters can be formed, as depicted in Figure 6(a) (Khairallah *et al.*, 2016; Liu *et al.*, 2015; Wang *et al.*, 2017). These larger-size spatters typically exceed 80 μm, contributing to an increase in top surface roughness, as evident in Figure 7(f).

Alongside spatter formation, the development of humps along the melt track at high-power conditions, e.g. P620_S1466.6, also impacts the top surface roughness, as exemplified in Figure 7 (c). As laser power increases, the molten liquid in the enlarged melt pool migrates from the center to the tail owing to the amplified Marangoni flow and enhanced recoil pressure, accumulating material at the rear of the melt pool. Upon solidification of the melt track, such accumulation forms the observed hump. Moreover, the periodic oscillation of the melt pool causes the liquid at the tail to change its flow direction periodically. This fluctuation induces corresponding material variations at the melt pool's tail, promoting the periodic formation of humps during the solidification process (Zhang *et al.*, 2024).

Compared with the protrusion height of the melt pool discontinuity [approximately 200 μm as depicted in Figure 6(a)], both the hump height (approximately 115 μm and 80 μm from Figures 6(b) and (c, respectively] and the spatter size [70 μm from Figure 6(f)] are significantly lower. Consequently, despite the occurrence of spatter and hump formation at the 620 W condition, the increase in laser power effectively smoothens the top surface by mitigating the melt pool discontinuity. In between, at 440 W conditions, a blend of features akin to those observed at 260 and 620 W conditions manifests on the top surface, which can be observed in Figures 6(b) and (e). A combination of the melt pool discontinuity, hump and spatter collectively influence the top surface quality, resulting in intermediate Sa values of 19.17 μm and 13.84 μm for P440_S1466.6 and P440_S1100, respectively (Figure 8).

3.3 Scanning speed on melt pool morphology and top surface quality

Figure 9(a) and (b), show the melt pool width and depth under varying scanning speeds at fixed laser power 260 and 620 W. Observing the same laser power, the melt pool width and depth decrease with an increase in scanning speed. Higher scanning speeds, corresponding to lower energy density, reduce the laser-matter interaction time. The reduced energy inputs, therefore, lead to smaller melt pool dimensions.

Figure 8 The Sa for top surfaces with varying laser power for fixed scanning speeds

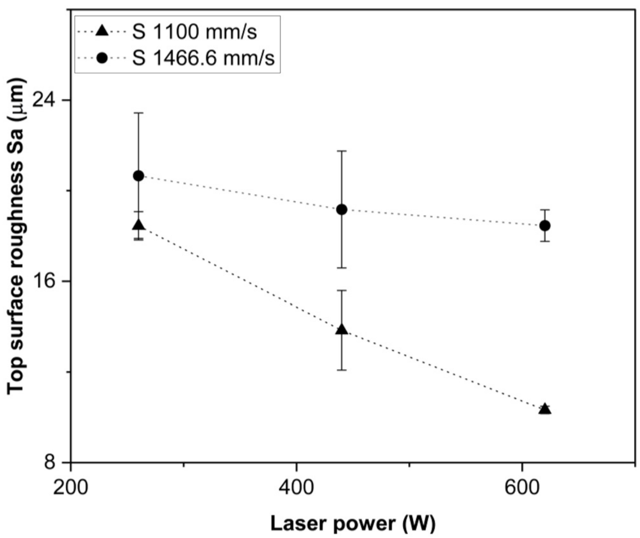

Source: Authors' own work

Figure 10 shows the top surface topography of the highest and lowest scanning speed conditions at the fixed laser power of 260 and 620 W, namely, P260_S1466.6, P260_S520, P620_S3100, and P620_S1100. In addition to the melt pool discontinuity, periodic humps are observed in Figure 10(a) and (c) . The formation of such hump within a discontinuous melt track is typically dominated by the Plateau–Rayleigh instability (DebRoy *et al.*, 2018; Gusarov and Smurov, 2010; Tian *et al.*, 2017; Yadroitsev *et al.*, 2010). When the ratio of the melt pool width to the length is small, the melt pool tends to adopt a spherical shape to minimize its surface energy. The critical value of the ratio was suggested by Yadroitsev *et al.* (2010):

$$\frac{\pi D}{L} > \sqrt{\frac{2}{3}} \tag{5}$$

where D is the melt pool width and L is the melt pool length.

The melt pool width/length ratio (D/L) was not directly measured due to the significant overlaps between tracks. Instead, the melt pool tail angle was utilized as an estimator, where a smaller melt pool tail angle represents the lower D/L ratio when the melt width is comparable or smaller (Zhang and Yuan, 2022). Measured from Figure 10(a) and (b), the tail angle of the melt pool for P260_S1466.6 is approximately 28°, smaller than approximately 39° in P260_S520. This observation implies that the D/L ratio is lower at a higher scanning speed. The melt pool width reduction (the melt pool width of P260_S520 is 189.56 μm, and the melt pool width of P260_S1466.6 is 85.45 μm) and the melt pool length elevation with the scanning speed increasing (Leung *et al.*, 2018; Zhang *et al.*, 2024) provide the reasons for this phenomenon.

At low-speed conditions, the increase in the melt pool width/length ratio diminishes the likelihood of the Plateau–Rayleigh instability and melt pool discontinuity on the top surface, contributing to its smoother appearance, as evidenced in Figures 10(b) and (d). Figure 11 quantifies the Sa for samples with fixed 260 and 620 W conditions. The Sa value increases with the rising scanning speed while maintaining constant laser power. Linear regression was assumed to assess the Sa with scanning speed. The slope for the cases with the laser power of 260 W is estimated at 0.0079 μm/(mm/s) in Figure 11(a), whereas 0.0064 μm/(mm/s) for cases in Figure 11(b) with the power of 620 W. This indicates that Sa is more sensitive to the variation of scanning speed at low laser power conditions. Under high laser power conditions (620 W), as discussed previously, high melt pool stability is provided by large melt pool dimensions and better wetting conditions, weakening the impact of high speed on top surface roughness and leading to the lower variation slope at 620 W condition.

3.4 VED with melt pool morphology and top surface roughness

Melt pool morphologies at cross-sections for different energy densities are shown in Figure 12. Each row corresponds to the identical VED with different laser power and scanning speed, while each column corresponds to the same laser power with different laser scanning speeds. Consistent with the observation in Figure 4, the melt pool dimensions exhibit an increase, and the melt pool cross-sectional shape transforms from an ellipse shape to a half-ellipse configuration as the scanning speed decreases (VED increases), as shown in each column of Figure 12.

Figure 13 illustrates the relationship between melt pool width and depth with laser power under various VED conditions. Both the width and depth of the melt pool exhibit an increase with higher laser power and scanning speed under constant VED conditions. An elevated laser power contributes to a higher peak melt pool temperature while maintaining a constant input energy density. Concurrently, the reduced heat diffusion time associated with higher scanning speeds facilitates heat accumulation in the melt region, ultimately leading to larger melt pool dimensions.

To illustrate the surface characteristics further, Figure 14 shows the top surface topography under different VEDs. Each column keeps the same VED, namely, 66.7 J/mm^3, 100 J/mm^3, 133.3 J/mm^3 and 166.7 J/mm^3, with increased laser power and scanning speed. Each row keeps the same laser power with reduced laser speed. Figure 15 quantifies the Sa for the conditions displayed in Figure 14. In each group where the VEDs are 100 J/mm^3, 133.3 J/mm^3, 166.7 J/mm^3, the Sa initially decreases and subsequently rises up with the increase in scanning speed and laser power at a fixed VED. The melt pool morphology and top surface topography exhibit similar features in these three groups, as illustrated in the three right columns of Figure 14 (three bottom rows in Figure 12). For instance, in VED of 133.3 J/mm^3 group, a relatively high Sa (16.88 μm) is dominated by the melt pool discontinuity and attached powders for P80_S200 condition, as shown in Figure 14(g). With the power and speed increase, the expanded melt pool dimensions reduce the melt pool discontinuity and smooth the top surfaces. The lowest Sa of 11.39 μm in this VED group is observed at P440_S1100 condition, where the top surface is dominated by continuous and smooth melt track [Figure 14(h)]. Beyond the lowest Sa point in this group, the Sa increases to 19.04 μm at P800_S2000 condition, owing to the hump formation with the increased power and speed, as shown in Figure 14(i). The increasing power not only creates higher recoil pressure but also leads to a higher thermal gradient in the melt pool, intensifying

Figure 9 Melt pool dimensions for fixed laser powers

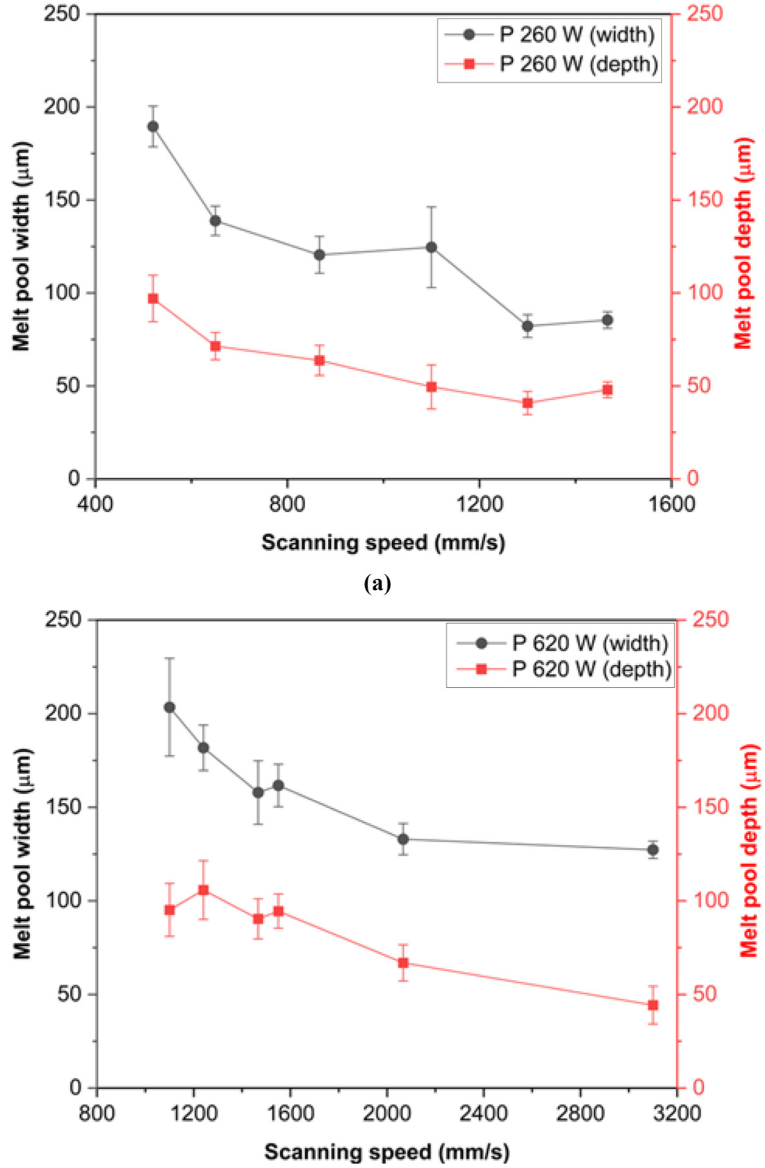

(a)

(b)

Notes: (a) 260 W; (b) 620 W
Source: Authors' own work

the Marangoni flow. Furthermore, the higher speed further elongates the melt pool, which enlarges the Plateau–Rayleigh instability, facilitating the hump formation. Similar transitional behaviors can also be observed in the VED of 100 *J/mm*^{3} group [Figure 14(d–f)].

In VED of 166.7 J/mm^3 group, all the samples consistently exhibit a Sa lower than 20 μm. High VED input generates larger melt pool dimensions with a substantial overlapping area and eliminates the melt pool discontinuity. The larger overlapping area not only remelts the features left from the adjacent track but only cooperates with the denudation effect, resulting in fewer spatter and hump formations with a stable melt pool, thus smoothing the top surface.

Finally, In VED 66.7 J/mm^3 group, the melt pool size remains insufficient to form a continuous melt track and flatten the top surface even with an increase in laser power and scanning speed, as shown in Figure 14(a–c). In addition, increased scanning speed worsens the melt pool instability. The possible material vaporization at the 800 W condition leads to the void formation on the top surface (Qiu *et al.*, 2015), further deteriorating the top surface quality, as shown in Figure 12(c)

Figure 10 The top surface topography for (a) P260_S1466.6, (b) P260_S520, (c) P620_S3100 and (d) P620_S1100

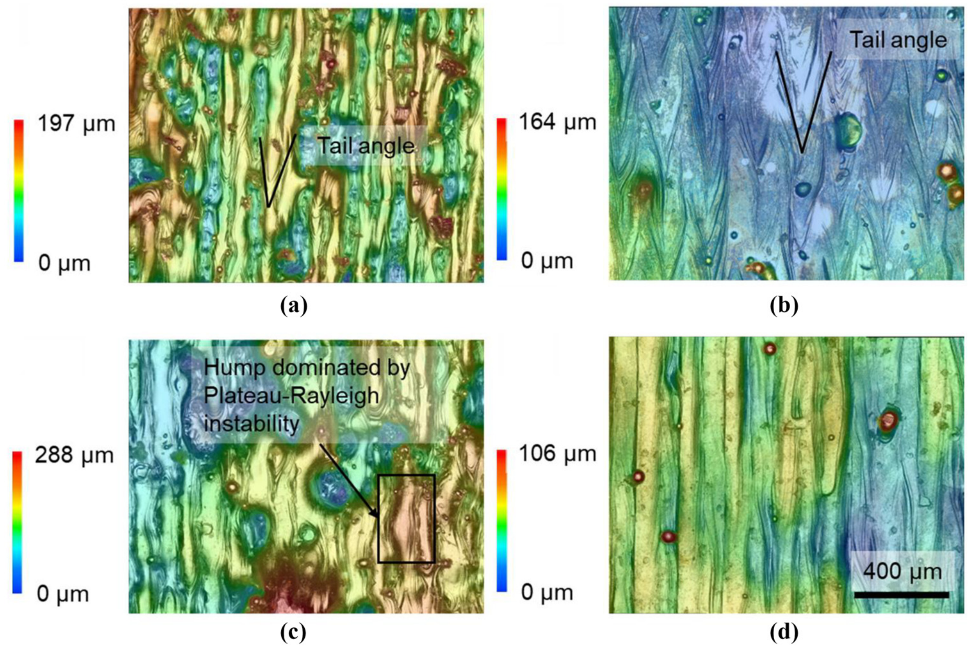

Source: Authors' own work

Figure 11 Top surface roughness Sa for fixed laser powers

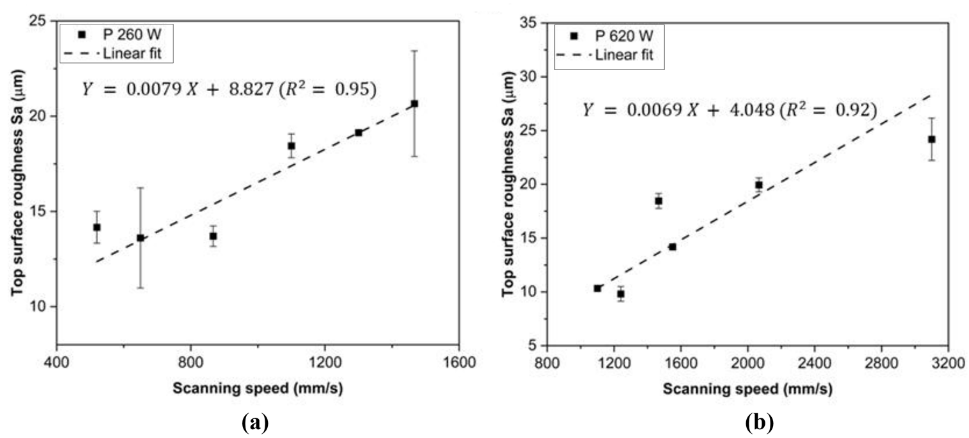

Notes: (a) 260 W; (b) 620 W
Source: Author's own work

and Figure 14(c). Consequently, P80_S400 exhibits the lowest Sa 18.23 μm within 66.7 J/mm^3 group.

Notably, for the lowest Sa condition within each VED group, the laser power shifts from low to high values as VED increases, as indicated in Figure 15. This trend implies that the optimal laser power required to achieve the best top surface quality in each VED group increases with increasing VED. This phenomenon can be attributed to the following underlying reasons: the velocity within the low VED group is higher than that in the high VED group under identical laser power conditions, consequently promoting increased Plateau–Rayleigh instability within the melt pool; and under high VED conditions, large melt pool overlapping area contributes to enhanced melt pool stability. Consequently, higher laser power and speed are necessitated to disrupt the stability and initiate the formation of the hump.

3.5 Features on top surface

Figure 16 is constructed to illustrate the melt pool morphology in the cross-section view along the laser scanning direction based on the current observations and literature studies that reveal the melt pool dynamics (Leung *et al.*, 2018, 2022; Qiu *et al.*, 2015), whereas Figure 17 is plotted to encapsulate the predominant features influencing top

Figure 12 The cross-sectional melt pool morphology for (a) P80_S400, (b) P440_S2200, (c) P800_S4000, (d) P80_S266.6, (e) P440_S1466.6, (f) P800_S2666.6, (g) P80_S200, (h) P440_S1100, (i) P800_S2000, (j) P80_S160, (k) P440_S880 and (l) P800_S1600

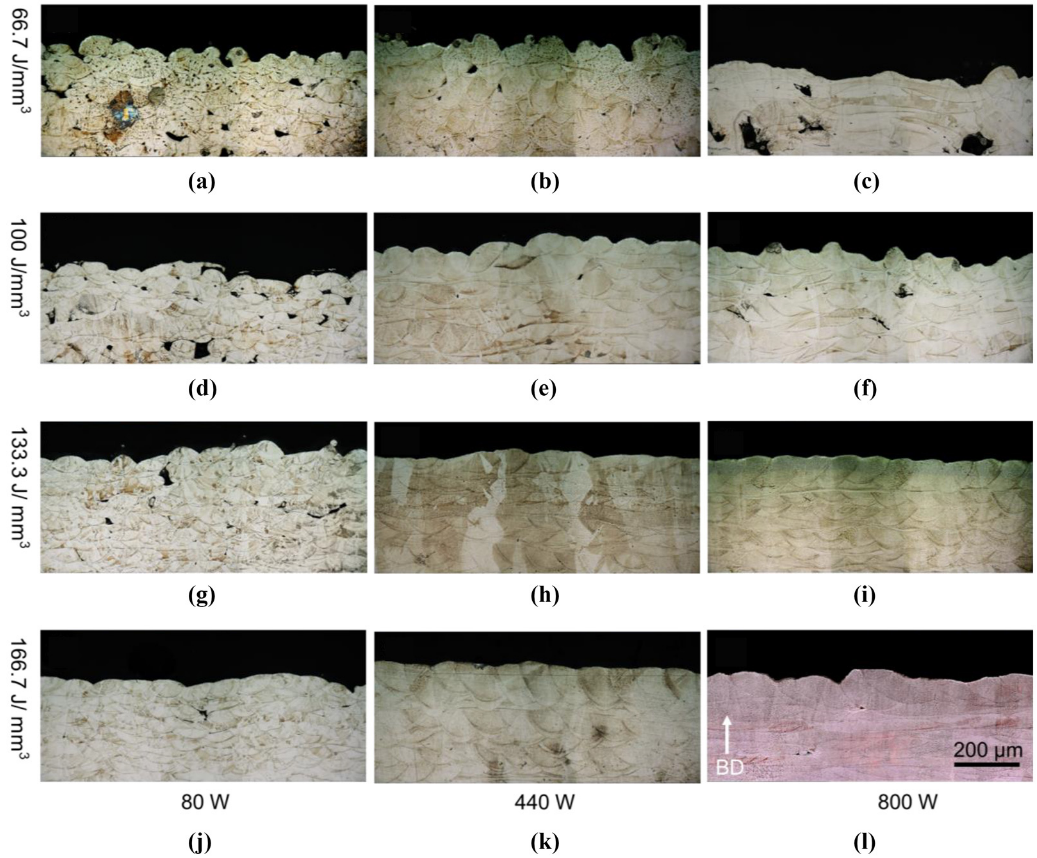

Source: Authors' own work

Figure 13 Melt pool dimensions at different VEDs

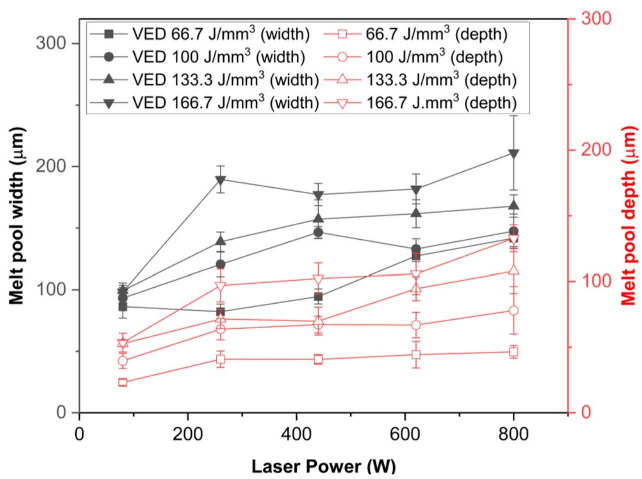

Source: Authors' own work

surface roughness under varied process conditions. At 80 W or 66.7 J/mm^3 conditions (indicated by orange dashed line in Figure 17), the top surface quality is dominated by melt pool discontinuity arising from constrained melt liquid volume. The cross-sectional morphology along the laser scanning direction of this discontinuous melt track is depicted in Figure 16(a), accompanied by a high Sa value exceeding 16.87 μm across all corresponding samples. With elevated laser power or VED conditions, the melt pool discontinuity diminishes. An adequate VED within a specified power range facilitates a cross-sectional half-ellipse shape with a smooth top surface quality (Sa <15 μm). Specifically, the optimal range is 260 W for 100 J/mm^3, 260 W to 620 W for 133.3 J/mm^3 and 260 W to 800 W for 166.7 J/mm^3, as shown in the blue dashed line region of Figure 17. In this region, a continuous melt pool with a smooth top surface is formed, as illustrated in Figure 16(b). However, hump formation could dominate the top surface quality when the scan speed exceeds 1,466.6 mm/s in 100 J/mm^3 and speed over 1550 mm/s at 133.3 J/mm^3 conditions (as indicated by the green dashed line in Figure 17). Figure 16(c) illustrates such behavior. Overall, the features that impact top surface quality can be summarized as:

- *Discontinuity of melt pool:* Under low power or VED conditions, the laser is insufficient to generate adequate liquid to form a stable melt pool. The surface tension breaks down the melt pool and leads to its discontinuity.
- *Hump:* Hump formation can be dominated by two mechanisms: First, when the scanning speed is high and the melt pool elongates, Plateau–Rayleigh instability disrupts the

Figure 14 Top surface topography for samples (a) P80_S400, (b) P440_S2200, (c) P800_S4000, (d) P80_S266.6, (e) P440_S1466.6, (f) P800_S2666.6, (g) P80_S200, (h) P440_S1100, (i) P800_S2000, (j) P80_S160, (k) P440_S880, (l) P800_S1600

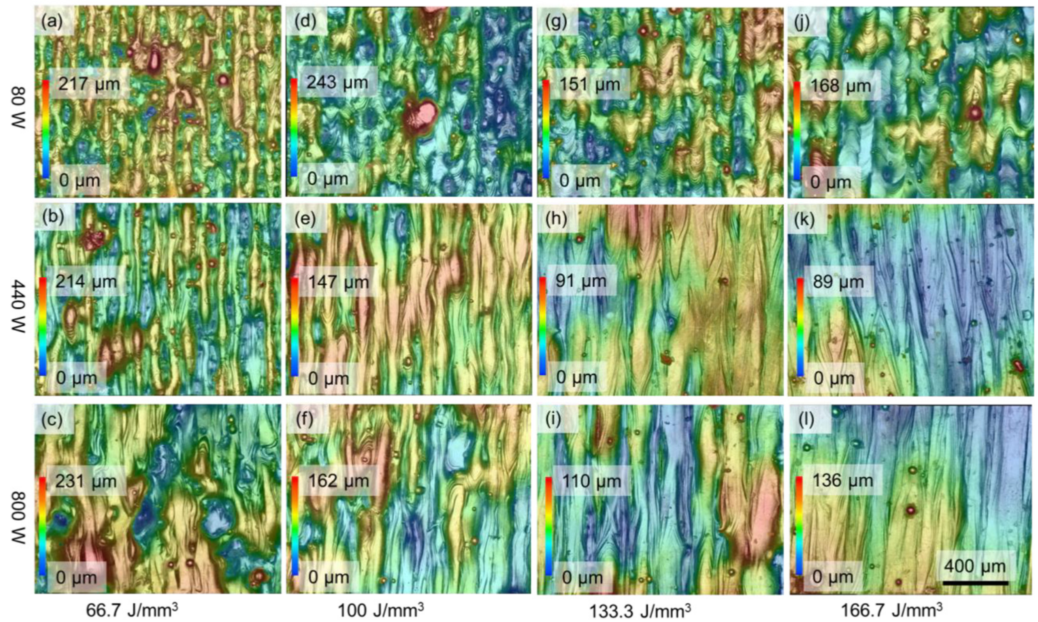

Source: Authors' own work

Figure 15 Top surface roughness with laser power for different VEDs

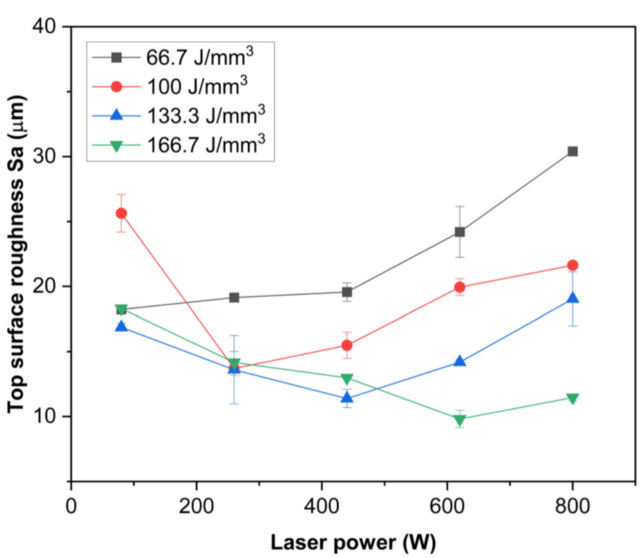

Source: Authors' own work

melt pool, preventing the liquid from flowing back and resulting in a hump. Second, under high VED conditions, intense recoil pressure and Marangoni flow push the liquid to the rear of the melt pool. The melted material accumulation forms the hump.

- *Spatter:* The droplet spatter is the metal liquid escaping from the melt pool once the recoil pressure is higher than the surface tension in the melt pool.

3.6 VED on build quality via porosity

Figure 18 presents optical images depicting cross-sectional views within the central region under different VED groups. Due to the consistency of the porosity level measured through cross-sectional optical images and Archimedes method detailed in the Appendix, only the data from cross-sectional images are presented in Figure 19. Note that the images for the upper region of specific subgroups are shown in Figure 12. Under VEDs of 66.7 J/mm^3 and 100 J/mm^3, irregular void shapes are evident within the bulk region of the samples [Figure 18(a–d) and (f),]. These pores manifest under insufficient VED conditions and maintain similar or smaller sizes than the dimensions of the melt pool, resulting from the lack of fusion. With increasing VED, the porosity level within the bulk diminishes significantly from a peak of 8.49% to approximately 0%, as shown in the third and fourth rows of Figure 18. As energy density escalates, the overlapping area between melt tracks expands alongside the elevation of melt pool dimensions (the third and fourth rows of Figure 12), consequently reducing porosity levels. Based on Figure 19, a VED of 133.3 J/mm^3 consistently produces the sample density over 99% in this research.

Small, round-shaped pores are also observed within the bulk region, notably in Figure 18(h), (n), (q) and (t), . These pores are commonly associated with gas trapped within the melt pool. In addition to rectifying the lack of fusion defects, the increase of VED contributes to reducing gas pore porosity within the samples (Dai and Gu, 2015b). The enlarged melt pool extends melt duration, allowing ample time for trapped gas to evacuate.

Figure 16 Illustration for the melt pool development under consistent VED with increased laser power and speed

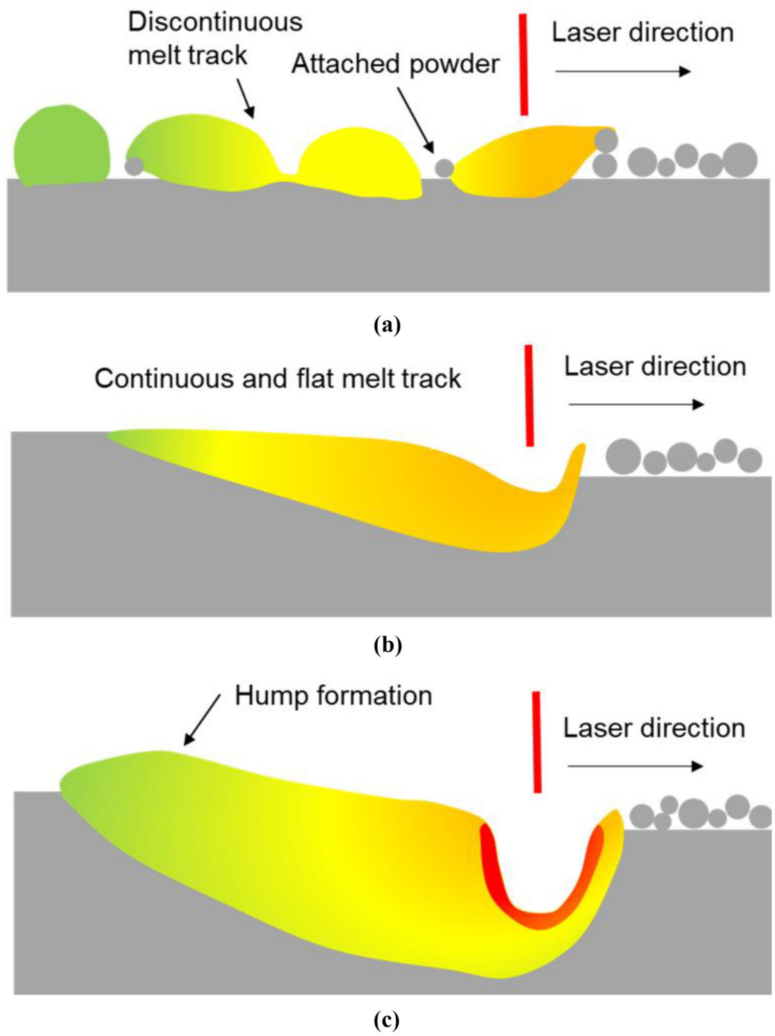

Source: Authors' own work

Figure 17 The processing parameter map for top surface roughness features

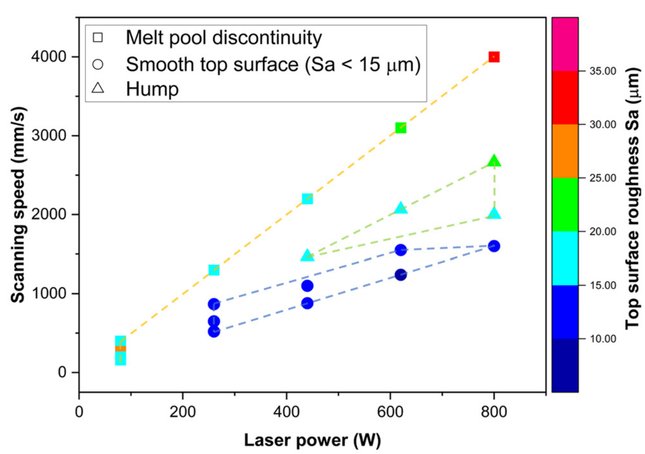

Source: Authors' own work

Figure 18 Cross-sectional views for pores under various VEDs

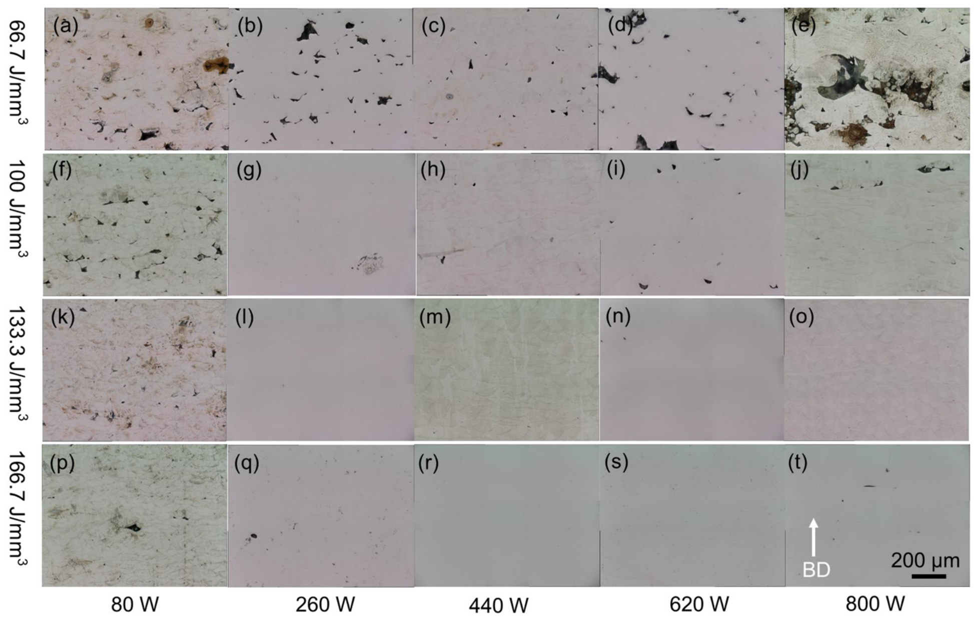

Source: Authors' own work

Additionally, elevated melt pool temperatures reduce liquid viscosity, facilitating gas escape.

The occurrence of large irregular voids, approximately 100 μm in size, in both the bulk [Figure 18(e)] and top region [Figure 12(c)] are notable in the P800_S4000 sample, exhibiting the highest porosity level (8.5%) with the VED of 66.7 J/mm^3. These voids most likely result from multiple factors: the low input VED not only leads to a lack of fusion defects but also triggers substantial material vaporization under high-power laser irradiation and results in melt pool instability at high scanning speeds (Dai and Gu, 2015b; Khairallah *et al.*, 2016; Qiu *et al.*, 2015). The high-power laser induces droplet spatter and denudation, leading to material loss from the melt pool. This combination of material vaporization and spatter ejection results in an insufficient material supply necessary for achieving fully dense prints. Concurrently, the Plateau–Rayleigh instability of the melt pool, leading to the melt pool dimensions variation along the scan tracks, which further results in the uneven powder distribution for the subsequent layer, exacerbates the void formation process.

At 800 W conditions, using a higher VED (associated with slower scanning speeds) results in an expansion of melt pool width and a reduction in melt pool length. This phenomenon effectively mitigates the Plateau–Rayleigh instability while augmenting the overlapping area, enhancing top surface quality. As discussed previously, the increased overlapping region interacts with the denudation effect, reducing laser absorption and mitigating excessive material vaporization. These collaborative effects, combined with smoother top surface characteristics and more uniform powder distribution in subsequent layers, lead to the absence of both lack of fusion pores and keyhole pores within the higher VED region under 800 W conditions.

Figure 19 Porosity under different VEDs

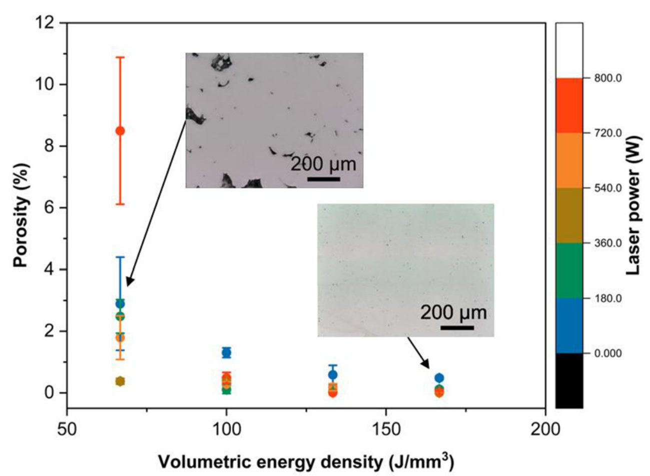

Source: Authors' own work

3.7 Top surface roughness on porosity level and printability

The characteristics of the melt pool play a crucial role in determining both the quality of the top surface and the occurrence of defects within the bulk material. The top surface roughness, thereby, may serve as an indicator of melt pool stability and the extent of defects present in the prints. During the printing process, the quality of the top surface governs the distribution of powder for subsequent layers. Elevated features within the melt pool, such as humps and spatters, can impede the even spreading of powder, causing powder absence at those locations. Conversely, depressed regions on the top surface, arising from melt pool discontinuities and Plateau–Rayleigh instability, lead to thicker powder areas for the next layer.

These uneven powder distributions can also contribute to the void formation within the bulk material.

In Figure 20, the correlation between porosity level and top surface roughness is illustrated. The plot indicates that a low top surface roughness corresponds to favorable printability, evidenced by low porosity levels (density over 99%). As illustrated in Figure 12(h–i) and (k), Figure 14(h–i) and (k), and Figure 18(m), (o) and (r), this outcome is facilitated by adequately sized, cross-sectionally half-elliptical melt pools. Besides, as marked in Figure 20, the high-density samples can also be attained under sufficient VED conditions with a rough top surface. As shown in Figure 12(f), Figure 14(f) and Figure 18(j), sufficient VED overcomes the humps and guarantees the P800_S2666.6 with a density 99.5%, even with a high Sa value 21.63 μm. On the contrary, at a low VED (66.7 J/mm^3), the top surface led by melt pool discontinuity further heightens the likelihood of roughness, promoting lack of fusion, as evidenced in Figure 12(a–c), Figure 14(a–c) and Figure 18(a), (c) and (e), The optimal parameters for achieving high-quality top surfaces (9.82 μm) and minimal porosity level (99% density) are determined to be P620_S1240 in this study.

In summary, a stable melt pool with favorable wetting conditions, achieved by adequate VED (higher than 100 J/mm^3 in this study), exhibits sufficient dimensions and a cross-sectional half-ellipse shape, contributing to both good top surface quality and high bulk density in the final product.

4. Conclusions

The effects of processing parameters on top surface roughness, melt pool morphology and porosity level are investigated in this study with a detailed examination of the top surface characteristics. Alongside summarizing the key features, such as humps, spatters and melt pool discontinuities, that significantly influence top surface quality, the relationship between top surface quality and porosity levels is revealed. The following conclusions are drawn from this study:

- Under consistent laser scanning speeds, the melt pool dimensions increase, and top surface roughness decreases with an increase in power from 260 W to 620 W, where the melt pool shape transforms from a discontinuous track to a continuous cross-sectional half-ellipse shape. Comparing the two groups with laser speeds of 1,466.6 mm/s and 1,100 mm/s, the low-speed case (high VED) widens the melt pool width but not the depth due to enhanced Marangoni flow and denudation effect.
- Under consistent laser power levels, the melt pool dimensions decrease, and top surface roughness increases with an elevation of speed from 520 mm/s to 3,100 mm/s. The sensitivity of top surface roughness to laser speed is more pronounced under low power conditions, exemplified by a steeper increase in Sa at 260 W compared to 620 W. This observation implies that enhanced stability in the melt pool is achieved under high power conditions, attributed to improved wetting and a larger overlapping region.
- Under conditions of low VED (66.7 J/mm^3), the melt pool track exhibits discontinuity, attributed to inadequate VED input, thereby yielding a rough top surface. As both scan speed and power increase, the Plateau–Rayleigh instability amplifies within the discontinuous track, further worsening the roughness of the top surface. Conversely, at a higher VED exceeding 100 J/mm^3, the interplay of increasing power and speed eliminates melt pool discontinuity, fostering the formation of a smooth top surface melt pool and consequently reducing top surface roughness. Subsequent increments in power and speed, however, result in the periodic formation of humps on the top surface, contributing to an increase in top surface roughness.
- The power required to attain the minimum top surface roughness within different VED groups exhibits a positive correlation with VED: a higher power is required to achieve minimal surface roughness at a high VED. This correlation can be elucidated by the presence of improved wetting conditions and a larger overlapping region, particularly prevalent in higher VED conditions.
- The fulfillment of a fully dense sample, reaching approximately 99%, can be realized through two distinct surface characteristics: a smooth top surface (e.g., Sa < 15 μm) or a rough surface dominated by humps at high VED (over 133.3 J/mm^3). In contrast, a rough top surface displaying melt pool discontinuity suggests the potential formation of porosity in the bulk. This study highlights that P620_S1240 yields the optimal top surface quality and the lowest porosity level with the VED 166.7 J/mm^3.

Through the correlation of top surface characteristics and the quantification of roughness under various process conditions, this study presents a promising approach to assessing porosity levels during printing by analyzing surface topography. With the utilization of optical cameras and profilometers, it potentially offers an additional tool for advancing in-situ monitoring for defect control in L-PBF.

Figure 20 Porosity versus top surface roughness Sa

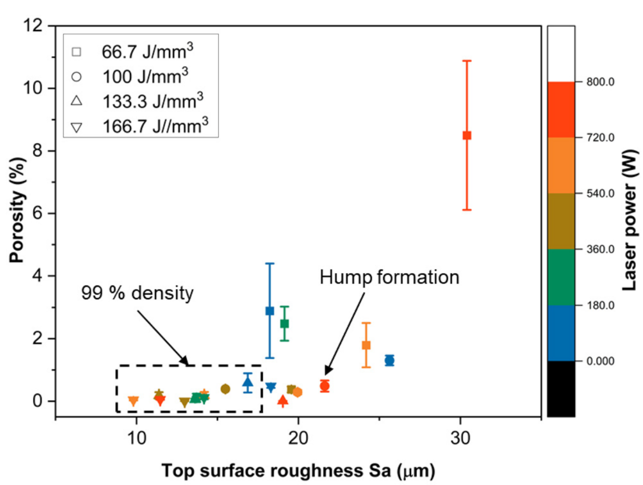

Source: Authors' own work

References

Al Aridi, R., DiNova, V., Zhang, T., Karna, S., Yuan, L., Krentz, T., Hitchcock, D., *et al.* (2024), "Characterization of defects in additively manufactured materials from mechanical properties", *Materials Science and Engineering: A, Elsevier B.V.* Vol. 898, p. 146390, doi: 10.1016/j.msea.2024.146390.

Bauereiß, A., Scharowsky, T. and Körner, C. (2014), "Defect generation and propagation mechanism during additive manufacturing by selective beam melting", *Journal of Materials Processing Technology, Elsevier B.V.* Vol. 214 No. 11, pp. 2522-2528, doi: 10.1016/j.jmatprotec.2014.05.002.

Cabanettes, F., Joubert, A., Chardon, G., Dumas, V., Rech, J., Grosjean, C. and Dimkovski, Z. (2018), "Topography of as built surfaces generated in metal additive manufacturing: a multi scale analysis from form to roughness", *Precision Engineering, Elsevier*, Vol. 52, pp. 249-265, doi: 10.1016/j.precisioneng.2018.01.002.

Calignano, F., Manfredi, D., Ambrosio, E.P., Iuliano, L. and Fino, P. (2013), "Influence of process parameters on surface roughness of aluminum parts produced by DMLS", *The International Journal of Advanced Manufacturing Technology*, Vol. 67 Nos 9/12, pp. 2743-2751, doi: 10.1007/s00170-012-4688-9.

Chen, H. and Yan, W. (2020), "Spattering and denudation in laser powder bed fusion process: multiphase flow modelling", *Acta Materialia, Elsevier Ltd*, Vol. 196, pp. 154-167, doi: 10.1016/j.actamat.2020.06.033.

Cook, P.S. and Murphy, A.B. (2020), "Simulation of melt Pool behaviour during additive manufacturing: underlying physics and progress", *Additive Manufacturing, Elsevier*, Vol. 31, p. 100909, doi: 10.1016/j.addma.2019.100909.

Cook, P.S. and Ritchie, D.J. (2023), "Determining the laser absorptivity of Ti-6Al-4V during laser powder bed fusion by calibrated melt Pool simulation", *Optics and Laser Technology, Elsevier Ltd*, Vol. 162, p. 109247, doi: 10.1016/j.optlastec.2023.109247.

Dai, D. and Gu, D. (2015a), "Effect of metal vaporization behavior on keyhole-mode surface morphology of selective laser melted composites using different protective atmospheres", *Applied Surface Science, Elsevier B.V*, Vol. 355, pp. 310-319, doi: 10.1016/j.apsusc.2015.07.044.

Dai, D. and Gu, D. (2015b), "Tailoring surface quality through mass and momentum transfer modeling using a volume of fluid method in selective laser melting of TiC/AlSi10Mg powder", *International Journal of Machine Tools and Manufacture, Elsevier*, Vol. 88, pp. 95-107, doi: 10.1016/j.ijmachtools.2014.09.010.

DebRoy, T., Wei, H.L., Zuback, J.S., Mukherjee, T., Elmer, J.W., Milewski, J.O., Beese, A.M., *et al.* (2018), "Additive manufacturing of metallic components – process, structure and properties", *Progress in Materials Science, Pergamon*, Vol. 92, pp. 112-224, doi: 10.1016/J.PMATSCI.2017.10.001.

Fischer, P., Romano, V., Weber, H.P., Karapatis, N.P., Boillat, E. and Glardon, R. (2003), "Sintering of commercially pure titanium powder with a Nd: YAG laser source", *Acta Materialia*, Vol. 51 No. 6, pp. 1651-1662, doi: 10.1016/S1359-6454(02)00567-0.

Fu, Y., Downey, A.R.J., Yuan, L., Zhang, T., Pratt, A. and Balogun, Y. (2022), "Machine learning algorithms for defect detection in metal laser-based additive manufacturing: a review", *Journal of Manufacturing Processes, Elsevier Ltd*, Vol. 75, pp. 693-710, doi: 10.1016/j.jmapro.2021.12.061.

Ghosh, S., Ma, L., Levine, L.E., Ricker, R.E., Stoudt, M.R., Heigel, J.C. and Guyer, J.E. (2018), "Single-track melt-pool measurements and microstructures in Inconel 625", *JOM*, Vol. 70 No. 6, pp. 1011-1016, doi: 10.1007/s11837-018-2771-x.

Gu, D. and Shen, Y. (2009), "Balling phenomena in direct laser sintering of stainless steel powder: metallurgical mechanisms and control methods", *Materials & Design, Elsevier*, Vol. 30 No. 8, pp. 2903-2910, doi: 10.1016/J.MATDES.2009.01.013.

Gusarov, A.V. and Smurov, I. (2010), "Modeling the interaction of laser radiation with powder bed at selective laser melting", *Physics Procedia*, Vol. 5 No. PART 2, pp. 381-394, doi: 10.1016/j.phpro.2010.08.065.

Hu, J.C., Yang, K., Wang, Q.Y., Zhao, Q.C., Jiang, Y.H. and Liu, Y.J. (2024), "Ultra-long life fatigue behavior of a high-entropy alloy", *International Journal of Fatigue, Elsevier Ltd*, Vol. 178, p. 108013, doi: 10.1016/j.ijfatigue.2023.108013.

Jing, G. and Wang, Z. (2021), "Defects, densification mechanism and mechanical properties of 300M steel deposited by high power selective laser melting", *Additive Manufacturing, Elsevier B.V*, Vol. 38, p. 101831, doi: 10.1016/j.addma.2020.101831.

Khairallah, S.A., Anderson, A.T., Rubenchik, A. and King, W.E. (2016), "Laser powder-bed fusion additive manufacturing: physics of complex melt flow and formation mechanisms of pores, spatter, and denudation zones", *Acta Materialia, Elsevier Ltd*, Vol. 108, pp. 36-45, doi: 10.1016/j.actamat.2016.02.014.

Le, T.N. and Lo, Y.L. (2019), "Effects of sulfur concentration and Marangoni convection on melt-pool formation in transition mode of selective laser melting process", *Materials and Design, The Authors*, Vol. 179, p. 107866, doi: 10.1016/j.matdes.2019.107866.

Lei, T., Rong, Y., Xu, J. and Huang, Y. (2018), "Experiment study and regression analysis of molten pool in laser welding", *Optics and Laser Technology*, Elsevier Ltd, Vol. 108, pp. 534-541, doi: 10.1016/j.optlastec.2018.07.053.

Leung, C.L.A., Luczyniec, D., Guo, E., Marussi, S., Atwood, R.C., Meisnar, M., Saunders, B., *et al.* (2022), "Quantification of interdependent dynamics during laser additive manufacturing using X-Ray imaging informed multi-physics and multiphase simulation", *Advanced Science*, Vol. 9 No. 36, pp. 1-15, doi: 10.1002/advs.202203546.

Leung, C.L.A., Marussi, S., Atwood, R.C., Towrie, M., Withers, P.J. and Lee, P.D. (2018), "In situ X-ray imaging of defect and molten pool dynamics in laser additive manufacturing", *Nature Communications*, Vol. 9 No. 1, pp. 1-9, doi: 10.1038/s41467-018-03734-7.

Leung, C.L.A., Marussi, S., Towrie, M., Atwood, R.C., Withers, P.J. and Lee, P.D. (2019), "The effect of powder oxidation on defect formation in laser additive manufacturing", *Acta Materialia, Acta Materialia Inc*, Vol. 166, pp. 294-305, doi: 10.1016/j.actamat.2018.12.027.

Liao, D., Zhu, S.P., Keshtegar, B., Qian, G. and Wang, Q. (2020), "Probabilistic framework for fatigue life assessment of notched components under size effects", *International Journal of Mechanical Sciences, Elsevier Ltd*, Vol. 181, doi: 10.1016/j.ijmecsci.2020.105685.

Liu, W. and DuPont, J.N. (2004), "Effects of melt-Pool geometry on crystal growth and microstructure development in laser surface-melted superalloy single crystals: mathematical modeling of single-crystal growth in a melt Pool (part I)", *Acta Materialia*, Vol. 52 No. 16, pp. 4833-4847, doi: 10.1016/j.actamat.2004.06.041.

Liu, Y., Yang, Y., Mai, S., Wang, D. and Song, C. (2015), "Investigation into spatter behavior during selective laser melting of AISI 316L stainless steel powder", *Materials and Design*, Elsevier B.V, Vol. 87, pp. 797-806, doi: 10.1016/j.matdes.2015.08.086.

Maleki, E., Bagherifard, S. and Guagliano, M. (2023), "Correlation of residual stress, hardness and surface roughness with crack initiation and fatigue strength of surface treated additive manufactured AlSi10Mg: experimental and machine learning approaches", *Journal of Materials Research and Technology*, *The Authors*, Vol. 24, pp. 3265-3283, doi: 10.1016/j.jmrt.2023.03.193.

Matthews, M.J., Guss, G., Khairallah, S.A., Rubenchik, A.M., Depond, P.J. and King, W.E. (2016), "Denudation of metal powder layers in laser powder bed fusion processes", *Acta Materialia*, *Acta Materialia Inc*, Vol. 114, pp. 33-42, doi: 10.1016/j.actamat.2016.05.017.

Mills, K.C. and Keene, B.J. (1990), "Factors affecting variable weld penetration", *International Materials Reviews*, Vol. 35 No. 1, pp. 185-216, doi: 10.1179/095066090790323966.

Mumtaz, K. and Hopkinson, N. (2009), "Top surface and side roughness of Inconel 625 parts processed using selective laser melting", *Rapid Prototyping Journal*, Vol. 15 No. 2, pp. 96-103.

Qiu, C., Panwisawas, C., Ward, M., Basoalto, H.C., Brooks, J. W. and Attallah, M.M. (2015), "On the role of melt flow into the surface structure and porosity development during selective laser melting", *Acta Materialia*, Elsevier Ltd, Vol. 96, pp. 72-79, doi: 10.1016/j.actamat.2015.06.004.

Rastan, H., Abdi, A., Hamawandi, B., Ignatowicz, M., Meyer, J.P. and Palm, B. (2020), "Heat transfer study of enhanced additively manufactured minichannel heat exchangers", *International Journal of Heat and Mass Transfer*, Elsevier Ltd, Vol. 161, doi: 10.1016/j.ijheatmasstransfer.2020.120271.

Semak, V. and Matsunawa, A. (1997), "The role of recoil pressure in energy balance during laser materials processing", *Journal of Physics D: Applied Physics*, Vol. 30 No. 18, pp. 2541-2552, doi: 10.1088/0022-3727/30/18/008.

Shi, X., Yan, C., Feng, W., Zhang, Y. and Leng, Z. (2020), "Effect of high layer thickness on surface quality and defect behavior of Ti-6Al-4V fabricated by selective laser melting", *Optics and Laser Technology*, Elsevier Ltd, Vol. 132, doi: 10.1016/j.optlastec.2020.106471.

Soderstrom, E. and Mendez, P. (2006), "Humping mechanisms present in high speed welding", *Science and Technology of Welding and Joining*, Vol. 11 No. 5, pp. 572-579, doi: 10.1179/174329306X120787.

Tang, C., Tan, J.L. and Wong, C.H. (2018), "A numerical investigation on the physical mechanisms of single track defects in selective laser melting", *International Journal of Heat and Mass Transfer*, Elsevier Ltd, Vol. 126, pp. 957-968, doi: 10.1016/j.ijheatmasstransfer.2018.06.073.

Tang, P., Wang, S., Duan, H., Long, M., Li, Y., Fan, S. and Chen, D. (2020), "The formation of humps and ripples during selective laser melting of 316l stainless steel", *The Journal of The Minerals, Metals & Materials Society*, Springer US, Vol. 72 No. 3, pp. 1128-1137, doi: 10.1007/s11837-019-03987-7.

Tangestani, R., Sabiston, T., Chakraborty, A., Muhammad, W., Yuan, L. and Martin, É. (2021), "An efficient track-scale model for laser powder bed fusion additive manufacturing: part 1-Thermal model", *Frontiers in Materials*, Vol. 8, pp. 1-14, doi: 10.3389/fmats.2021.753040.

Teng, C., Gong, H., Szabo, A., Dilip, J.J.S., Ashby, K., Zhang, S., Patil, N. *et al.* (2017), "Simulating melt pool shape and lack of fusion porosity for selective laser melting of cobalt chromium components", *Journal of Manufacturing Science and Engineering*, Vol. 139 No. 1, pp. 1-11, doi: 10.1115/1.4034137.

Thompson, S.M., Aspin, Z.S., Shamsaei, N., Elwany, A. and Bian, L. (2015), "Additive manufacturing of heat exchangers: a case study on a multi-layered Ti-6Al-4V oscillating heat pipe", *Additive Manufacturing*, Elsevier B.V, Vol. 8, pp. 163-174, doi: 10.1016/j.addma.2015.09.003.

Tian, Y., Tomus, D., Rometsch, P. and Wu, X. (2017), "Influences of processing parameters on surface roughness of Hastelloy X produced by selective laser melting", *Additive Manufacturing*, Elsevier B.V, Vol. 13, pp. 103-112, doi: 10.1016/j.addma.2016.10.010.

Triantaphyllou, A., Giusca, C.L., Macaulay, G.D., Roerig, F., Hoebel, M., Leach, R.K., Tomita, B., *et al.* (2015), "Surface texture measurement for additive manufacturing", *Surface Topography: Metrology and Properties*, Vol. 3 No. 2, doi: 10.1088/2051-672X/3/2/024002.

Wang, F., Wu, X.H. and Clark, D. (2011), "On direct laser deposited hastelloy X: dimension, surface finish, microstructure and mechanical properties", *Materials Science and Technology*, Vol. 27 No. 1, pp. 344-356, doi: 10.1179/026708309X12578491814591.

Wang, D., Wu, S., Fu, F., Mai, S., Yang, Y., Liu, Y. and Song, C. (2017), "Mechanisms and characteristics of spatter generation in SLM processing and its effect on the properties", *Materials and Design*, Elsevier Ltd, Vol. 117, pp. 121-130, doi: 10.1016/j.matdes.2016.12.060.

Yadroitsev, I., Bertrand, P. and Smurov, I. (2007), "Parametric analysis of the selective laser melting process", *Applied Surface Science*, Vol. 253 No. 19, pp. 8064-8069, doi: 10.1016/j.apsusc.2007.02.088.

Yadroitsev, I., Gusarov, A., Yadroitsava, I. and Smurov, I. (2010), "Single track formation in selective laser melting of metal powders", *Journal of Materials Processing Technology*, Vol. 210 No. 12, pp. 1624-1631, doi: 10.1016/j.jmatprotec.2010.05.010.

Yadroitsev, I., Krakhmalev, P., Yadroitsava, I., Johansson, S. and Smurov, I. (2013), "Energy input effect on morphology and microstructure of selective laser melting single track from metallic powder", *Journal of Materials Processing Technology*, Elsevier B.V, Vol. 213 No. 4, pp. 606-613, doi: 10.1016/j.jmatprotec.2012.11.014.

Yakout, M., Cadamuro, A., Elbestawi, M.A. and Veldhuis, S. C. (2017), "The selection of process parameters in additive manufacturing for aerospace alloys", *International Journal of Advanced Manufacturing Technology*, Vol. 92 Nos 5/8, pp. 2081-2098, doi: 10.1007/s00170-017-0280-7.

Yang, J., Han, J., Yu, H., Yin, J., Gao, M., Wang, Z. and Zeng, X. (2016), "Role of molten Pool mode on formability, microstructure and mechanical properties of selective laser melted Ti-6Al-4V alloy", *Materials and Design, Elsevier Ltd*, Vol. 110, pp. 558-570, doi: 10.1016/j.matdes.2016.08.036.

Yin, H. and Emi, T. (2003), "Marangoni flow at the gas/melt interface of steel", *Metallurgical and Materials Transactions B*, Vol. 34 No. 5, pp. 483-493, doi: 10.1007/s11663-003-0015-z.

Young, Z.A., Guo, Q., Parab, N.D., Zhao, C., Qu, M., Escano, L. I., Fezzaa, K., *et al.* (2020), "Types of spatter and their features and formation mechanisms in laser powder bed fusion additive manufacturing process", *Additive Manufacturing, Elsevier*, Vol. 36, p. 101438, doi: 10.1016/j.addma.2020.101438.

Zhang, T. and Yuan, L. (2022), "Understanding surface roughness on vertical surfaces of 316 L stainless steel in laser powder bed fusion additive manufacturing", *Powder Technology, Elsevier*, Vol. 411, p. 117957, doi: 10.1016/J.POWTEC.2022.117957.

Zhang, Z., Zhang, T., Sun, C., Karna, S. and Yuan, L. (2024), "Understanding melt pool behavior of 316L stainless steel in laser powder bed fusion additive manufacturing", *Micromachines*, Vol. 15 No. 2, p. 170, doi: 10.3390/mi15020170.

Zhu, Y., Zhou, L., Wang, S., Zhang, C., Zhao, C., Zhang, L. and Yang, H. (2020), "On friction factor of fluid channels fabricated using selective laser melting", *Virtual and Physical Prototyping, Taylor & Francis*, Vol. 15 No. 4, pp. 496-509, doi: 10.1080/17452759.2020.1823093.

Appendix: Porosity measurements through the Archimedes method

The Archimedes method is employed to validate the porosity levels determined via cross-sectional optical images. The mass of samples immersed in water and in air is measured for each sample, facilitating the computation of relative density using equation (A1):

$$\rho = \frac{W_w * \rho_w}{W_w - W_a} \tag{A1}$$

where W_w represents the weight measurement in water, W_a is the weight measurement in air and ρ_w is the density of water (998 g/L). Three measurements were conducted, and the arithmetic mean was computed.

Figure A1 illustrates the disparity in relative density measured by the Archimedes method and cross-sectional images. Despite the variance, the discrepancy among different measurement methodologies remains minimal, constituting less than 5%. The divergence observed in the cross-sectional imaging results primarily stems from variations in pore distribution. Conversely, fluctuations in weight measurements and the presence of pores in proximity to the surface region elucidate the deviations observed in the results obtained via the Archimedes method.

Figure A1 The relative density measurements through different methods

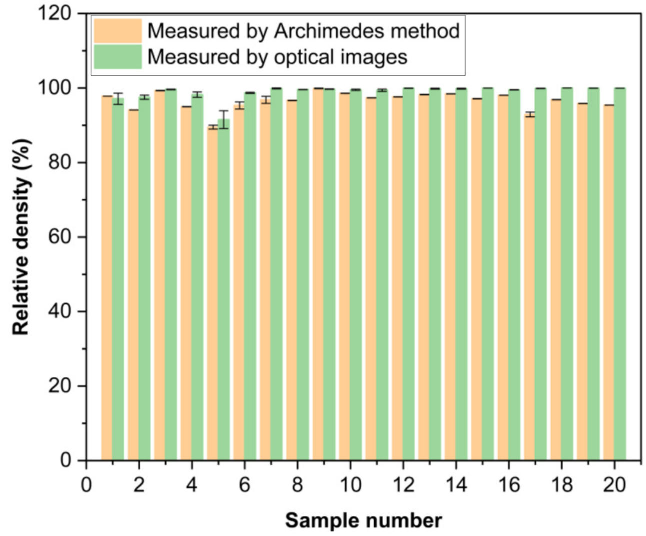

Source: Authors' own work

Corresponding author

Lang Yuan can be contacted at: langyuan@cec.sc.edu